

Epitaxial Engineering Strategy to Amplify Localized Surface Plasmon Resonance and Electrocatalytic Activity Enhancement in Layered Bismuth Selenide by Phosphorus Functionalization

Antony Samy Dennyson Savariraj,^[a] Ramu Manikandan,^[a] C. Justin Raj,^[b] Rajavel Velayutham,^[a] R. V. Mangalaraja,^[c, d] Jinsoo Park,^[e] Won-Je Cho,^{*[f]} and Byung Chul Kim^{*[a]}

Bismuth selenide (Bi_2Se_3) is an orderly layered material with large surface area and localized surface plasmon resonance (LSPR). The electrocatalytic profile of Bi_2Se_3 has been least explored for energy storage applications since its pristine form is handicapped with limited electrical conductivity. Here we report an epitaxial engineering strategy to manipulate the weak van der Waals forces to expand the interlayer spacing by intercalating phosphorus (P) atom by chemical vapor deposition (CVD) method. The obtained P intercalated Bi_2Se_3 ($\text{P@Bi}_2\text{Se}_3$) exhibited towering LSPR, increased carrier density bestowing ample active sites, enhanced ion diffusion and plentiful channels for the exodus of electrolyte. The potential of $\text{P@Bi}_2\text{Se}_3$ was examined for energy storage application which exhibited

battery like behavior with a specific capacity (C_s) of 194 C g^{-1} at 3 A g^{-1} current density against 121 C g^{-1} by $\text{Bi}_2\text{Se}_3/\text{NF}$ under identical condition and restored 88% of its initial specific capacity even after 5000 charge/discharge cycles. The hybrid supercapacitor (HSC) assembled using $\text{P@Bi}_2\text{Se}_3$ and O, N, S@AC as positive and negative electrodes exhibited a considerable specific capacitance, high specific energy (E_s) and specific power (P_s) with excellent stability for 10000 charge/discharge cycles. The surface and interfacial engineering strategy proposed here can be extended to tune plasmonic resonance and charge carrier energy density for the successful implementation of Bi_2Se_3 beyond energy storage applications.

Introduction

With graphene being the forerunner of layered materials, it unveiled several facets of material science with fascinating properties.^[1] Many materials mimicking graphene have drawn research focus in the recent past, with interesting features fitting them for serval applications from sensing to biomedical platform, extending to energy harvesting and storage applications. Their narrow bandgap, good thermal conductivity and environmental friendliness make them suitable candidates for thermoelectric applications, photodetector, sensors along with a wide array. Exfoliating the bulk layered material into single layer and few layers using different techniques including mechanical process opened new prospects to obtain two-dimensional (2D) materials with large surface area to volume ratio than their bulk counterparts.^[2,3] Furthermore, their significant features such as wide range of bandgap with tunability, optical absorption in longer wavelength,^[4-7] localized magnetic moments,^[4,8,9] and layered structures influenced anisotropic properties and their competence to accommodate host species thorough intercalation, make them preferable.^[10] Layered transition-metal chalcogenides are a class of materials which comprise of metals such as Mo, Co and chalcogens (X) such as S, Se and Te.^[11,12] The metal atoms are sandwiched by covalent bonds in between a pair of chalcogen atoms to form quintuple layer (Se–Bi–Se–Bi–Se) and the individual layers are held together via ‘van der Waals’ forces.^[13] The sheets formed in nanoscale by laminar stacking exhibit increased surface-to-

[a] Dr. A. D. Savariraj, Dr. R. Manikandan, R. Velayutham, Prof. B. C. Kim
Department of Advanced Components and Materials Engineering
Sunchon National University
255, Jungang-ro, Suncheon-si, Jellanamdo, 57922, Republic of Korea
E-mail: uunberry61@gmail.com

[b] Dr. C. J. Raj
Advanced Functional Nanohybrid Material Laboratory, Department of Chemistry
Dongguk University Seoul-Campus
Seoul, 04620, Republic of Korea

[c] Prof. R. V. Mangalaraja
Advanced Ceramics and Nanotechnology Laboratory
Department of Materials Engineering, Facultad de Ingeniería
Universidad de Concepción
Concepción 4070409, Chile

[d] Prof. R. V. Mangalaraja
Technological Development Unit (UDT)
University of Concepcion
Coronel Industrial Park, Coronel, Chile

[e] Prof. J. Park
Department of Advanced Aerospace Materials Engineering
Kyungwoon University
Gumi 39160, Republic of Korea

[f] Prof. W.-J. Cho
Department of Accelerator Application Research Division
Korea Atomic Energy Research Institute
181 Mirae-ro, Geoncheon-eup, Gyeongju, Gyeongbuk 38180, Republic of Korea
E-mail: wonje59@kaeri.re.kr

 Supporting information for this article is available on the WWW under
<https://doi.org/10.1002/batt.202100310>

volume ratio, catering Faradaic battery-type electrochemical behavior.^[14] This feature available in layered materials allows them to be used for energy storage applications.

Apart from noble metal, nanoparticles such as gold (Au), silver (Ag),^[15] many chalcogenides of copper (Cu)^[16,17] and bismuth (Bi)^[18] and their composites^[19] do possess localized surface plasmon resonance (LSPR). The layered metal chalcogenides particularly tend to bind to other metals possessing soft Lewis acid behavior with their open chalcogenide framework structure and chalcogenides' soft Lewis base nature.^[20,21] Layered architectures can be epitaxially engineered in several ways such as by doping and intercalation to alter their structure along c axis. The interlayer space available in layered materials provides space for intercalation of guest atoms and eventually facilitated the route for the charge transport.^[22] Similar to graphene, the 2D surface states of 3D bulk Bi₂Se₃ do have massless Dirac fermions to behave metallic with band gap between 0.3–0.35 eV, which otherwise be an insulator as bulk.^[23,24] The electromagnetic radiation can create plasmonic excitation layered architectures of Bi₂Se₃ and make LSPR more feasibly with quantum confinement.^[25]

In such layered structures, introduction of phosphorous (P) can be realized by means of epitaxial engineering;^[26] either it can be accommodated in between two chalcogens similar to the metal atoms,^[13] or accommodation by means of interaction in between the two neighboring Bi₂S₃ layers. Such epitaxial modification in layered materials exhibited better electrocatalytic profile particularly inclusion of P facilitated hydrogen evolution reaction (HER)^[27,28] with enhanced reversibility in H adsorption^[13] where the trapped protons act as base.^[29] P incorporated Bi₂Se₃ can benefit combinedly from Se and P, therefore P can be a perfect replacement for precious catalysts. Bismuth selenide (Bi₂Se₃) is a semiconducting metal chalcogenide belonging to V–VI groups,^[18,30] but least investigated due to its low electrochemical reversibility from poor conductivity and high-volume expansion in spite of its merits such as appreciable thermal conductivity and narrow bandgap.^[22] In order to improve the cyclability of Bi₂Se₃, several measures can be adopted and one such is intercalation of metal atom in between the individual Bi₂Se₃ layers. However, attempts to explore on exploiting stacked 3D bulk Bi₂Se₃ except exfoliation are not much ventured. With already established reports on the intercalation of lithium,^[31,32] we realized the intercalation of P in between the bismuth selenide layers can unfold new avenues. Upon intercalation of P, the existing localized surface plasmon resonance of Bi₂Se₃ is improved further which is reflected in its electrocatalytic activity owing to the increase in the charge carrier and carrier mobility as other layered materials.^[33,34]

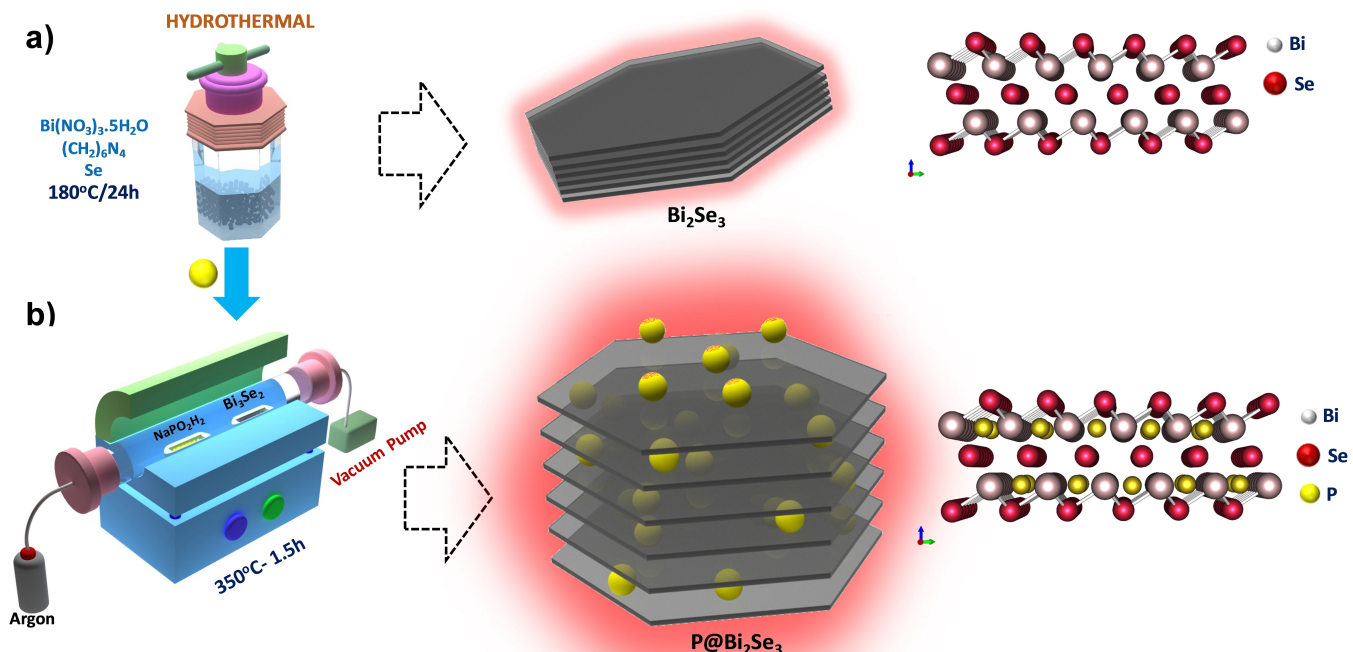
In this work we have presented one step hydrothermal synthesis of Bi₂Se₃ layers followed by P incorporation by chemical vapor deposition to obtain P@Bi₂Se₃. The obtained P@Bi₂Se₃ possessed superior electrocatalytic activity than pristine Bi₂Se₃ when employed as positive electrode material for supercapacitor. The three-electrode assembly made of P@Bi₂Se₃ delivered a specific capacity of 194 C g⁻¹ against 121 C g⁻¹ by Bi₂Se₃ whilst the hybrid supercapacitor (HSC) assembled using P@Bi₂Se₃ as positive and activated carbon (O,

N S@AC) from lima bean shells^[35] as negative electrodes delivered an energy density of 18.06 Wh kg⁻¹ corresponding to power density of 1550 W kg⁻¹ respectively under ideal condition. The HSC fabricated using P@Bi₂Se₃//O, N, S@AC composition exhibited battery like capacitive behavior with a well pronounced cyclic stability of 90.8% with excellent capacitance retention even beyond 10000 galvanostatic charge discharge cycles.

Results and Discussion

Firstly, layered Bi₂Se₃ were synthesized by hydrothermal method followed by surface phosphorization of the layered Bi₂Se₃ was carried out using chemical vapor deposition method as described in the experimental section. The schematic illustration of the entire procedure has been depicted in Scheme 1. In the recent past Bi₂Se₃ gained a great attention on account of its layered structure, its susceptibility to easy exfoliation and chemical modification to suit the research application requirement. In this regard, 2D exfoliated layers of Bi₂Se₃ and surface functionalized 3D bulk material are more preferred over the pristine 3D bulk Bi₂Se₃ owing to their improved catalytic performance after modification. The weak van der Waals interaction holds individual 2D Bi₂Se₃ layers to form a 3D stacked composition^[36] and therefore, apart from exfoliation, manipulation of physical characteristics of the layered 3D bulk Bi₂Se₃ to tune the properties for achieving tailor-made properties.

Such functionalized 3D bulk Bi₂Se₃ with surface modification and guest atoms intercalation facilitate electrocatalytic activity alike the exfoliate few layers of Bi₂Se₃. Similar to lithium (Li) and copper (Cu) intercalation, during phosphorization P will substitute the van der Waals voids of 2.3 Å^[31,37,38] altering carrier concentration and eventual charge transfer from intercalant. Also, the intercalation of phosphorous would bring in supplementary layers perpendicular to the c axis. Although electrochemical exfoliation and intercalation demonstrated several advantages in surface engineering of layered materials such being simple, eco-friendly and offering high precision by controlling different parameters,^[31,39–43] we adopted chemical vapor deposition (CVD) method for the intercalation of P since it can simultaneously improve the crystallinity. The structural elucidation in terms of crystal structure and phase purity of Bi₂Se₃ and P@Bi₂Se₃ is confirmed by X-ray diffraction (XRD) carried out at room temperature. The XRD spectra of Bi₂Se₃ (pink) and P@Bi₂Se₃ (dark blue) presented in Figure 1(a) display sharp peaks, indicative of highly pure phase with excellent crystallinity without any impurity. The family of planes observed in the pattern for Bi₂Se₃ sample [(006), (101), (015), (107), (018), (1010), (110), (0015), (021), (205), (1016), (0210), (1115), (125), (0216), (2110) and (300)] can be indexed to rhombohedral phase with R̄3m space group and hexagonal axis of ICDD card No:33-0214 with the following lattice parameters $a=b=4.1396 \text{ \AA}$, $c=28.6360 \text{ \AA}$, $\alpha=\beta=90^\circ$, $\gamma=120^\circ$.^[14,25,44] Additional tiny peaks found at 62.6° and 84.9° closely match with (0216) and (1120) planes of Bi₂Se₄.



Scheme 1. Schematic illustrations of a) hydrothermal synthesis of 3D Bi_2Se_3 and b) intercalation of P in layered Bi_2Se_3 by CVD process.

respectively, corresponding to ICDD card No:65-3694. Similarly, a couple of minute diffraction peaks of observed at 27.5° and 86.8° can be ascribed to (007) and (2016) planes of BiSe respectively pertaining ICDD card No:29-0246, however predominantly found Bi_2Se_3 phase is considered. The interaction of P in Bi_2Se_3 leads to the suppression and shifting of several peaks observed in Bi_2Se_3 and this can be elucidated by making an appropriate comparison. As seen in Figure 1(b) the peaks corresponding to (015), (1010), (110) and (0015) planes have undergone a shift towards the lower angle or left shift as indicated with blue color arrows. The peak corresponding to (0015) plane has undergone partial suppression besides a couple of peaks pertaining to (002) and (107) planes have undergone complete suppression as designated with green color arrow. The doublet peak ascribed to (015) plane is transformed into unified peak with higher intensity after intercalation of P while other peaks accredited to (1010) and (110) planes also have undergone an increase in their intensities. Certain peaks corresponding to (015), (1010), (110) and (0015) planes exhibited a shift toward lower angle to the tune of 0.3° - 0.6° in 2θ value, which is attributed to strain from planar stress, change in stoichiometry due to P intercalation as evidenced in other cases.^[38] The peaks pertaining to (015), (1010) and (110) planes undergo a decrease in their full width at half maximum values. The peaks with high intensity and sharp reflections evidence for the outstanding crystalline nature and excellent phase purity of the samples prepared after being subjected to annealing at 350°C during P intercalation. To supply further evidence for the peak shift due to P intercalation, the XRD spectrum of Bi_2Se_3 -A (annealed at 350°C

for 1.5 h under Ar atmosphere without $\text{NaPO}_2\text{H}_2 \cdot 2\text{H}_2\text{O}$) is compared with Bi_2Se_3 and $\text{P}@\text{Bi}_2\text{Se}_3$ (Figure S1a and b). The diffraction patterns of Bi_2Se_3 and Bi_2Se_3 -A almost overlap with each other except the variation in the intensity. The attainment of better crystallinity by Bi_2Se_3 -A, over $\text{P}@\text{Bi}_2\text{Se}_3$ can be made out from the increased intensity of the diffraction peaks belonging to Bi_2Se_3 -A, although peak shift is experienced only in $\text{P}@\text{Bi}_2\text{Se}_3$. Therefore, it is clear that the peak shift observed in $\text{P}@\text{Bi}_2\text{Se}_3$ resulted only from P intercalation and not due to the heat applied.

Bi_2Se_3 the Quintuple Layer (QL) measuring to a length of 7.15 \AA , comprises of a set of five monoatomic layers bonded covalently where Bi is sandwiched in between the chalcogenides in the order of Se-Bi-Se-Bi-Se.^[45] The van der Waals force acting between the two adjacent quintuple layer is weaker than the binding force acting within individual quintuple layer which lets easy accommodation of the guest atom (P) in two ways; i) in between the two Bi_2Se_3 layers causing increment in the c-axis lattice parameter and ii) replacement of Bi atoms and consequent decrease in the c-axis lattice parameter because of the smaller atomic radius (1.23 \AA) as compared to that of Bi (1.63 \AA). In either way it can result in crystal cells expansion.^[46] Figure 1(c) represents the UV-vis absorbance spectra of ethanol dispersed Bi_2Se_3 and $\text{P}@\text{Bi}_2\text{Se}_3$ samples. From the spectra, it can be observed that both the samples show a sharp peak at 268 nm and LSPR is present in the near-infrared (NIR) region as it is seen from the absorption even beyond 1200 nm , where oscillation of free carriers occurs.^[47] Inclusion of P has significantly increased the intensity of absorption spectrum ($\text{P}@\text{Bi}_2\text{Se}_3$) in the NIR region, and this further increases the LSPR

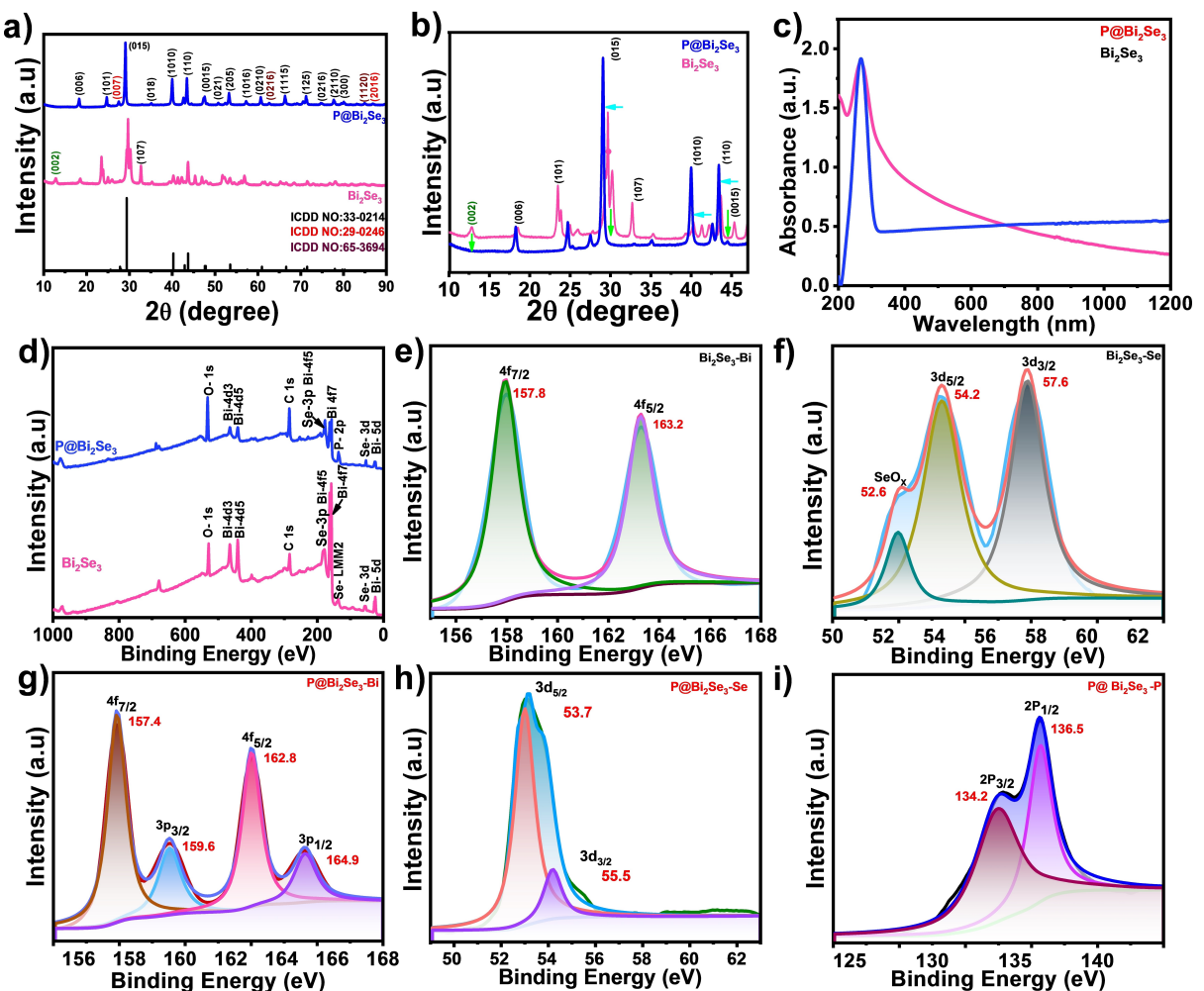


Figure 1. a) XRD patterns of Bi_2Se_3 and $\text{P}@\text{Bi}_2\text{Se}_3$ and b) magnified view showing a shift towards lower 2θ and peak suppression, XPS spectra of the Bi_2Se_3 and $\text{P}@\text{Bi}_2\text{Se}_3$, c) UV-vis absorbance spectra of ethanol dispersed Bi_2Se_3 and $\text{P}@\text{Bi}_2\text{Se}_3$ samples, d) wide survey scan spectra, high-resolution spectra of Bi_2Se_3 at e) bismuth region (Bi 4f), f) selenium region (Se 3d), high-resolution spectra of $\text{P}@\text{Bi}_2\text{Se}_3$ at g) bismuth region (Bi 4f), h) selenium region (Se 3d) and phosphorous region (P 2p).

profile of the sample. Here similar to phase transition, introduction of P could tune the free carrier concentration.^[16,48,49] Incorporation of P in to layered Bi_2Se_3 can increase the population of free electrons in the conduction band leading to escalation of exiting LSPR in the NIR region. To draw information on the chemical state of elements X-ray photoelectron spectroscopy (XPS) was carried out and the exact chemical composition and energy states were analyzed. The wide survey scan spectrum for Bi_2Se_3 and $\text{P}@\text{Bi}_2\text{Se}_3$ presented in Figure 1(d) indicates the presence of Bi , Se and P confirming the purity of the prepared samples. However, two tiny, uncommon peaks corresponding to oxygen (O) and carbon (C) at 531.8 and 284.6 eV respectively arise from moisture adsorption and hydrocarbon contamination due to exposure to atmosphere and the absence of peaks pertaining to other elements evidence for the purity of the samples further.^[50–52] There is an overlap of peaks for Se LMM²^[53] at a binding energy of 136.2 eV for Bi_2Se_3 and P 2p at 136.5 eV for $\text{P}@\text{Bi}_2\text{Se}_3$, nonetheless the intensity of the peak in the case of P 2p for $\text{P}@\text{Bi}_2\text{Se}_3$ with an additional hump is slightly higher as

compared to that of Se LMM² for Bi_2Se_3 . Similar peak at around 136 eV has been observed even in pristine Bi_2Se_3 ^[18,45,54,55] and $\text{Bi}_2\text{Se}_{3-x}\text{Te}_x$.^[45,56] A set of peaks at 398 and 678 eV corresponding Se -LMM²^[57] and 4p of Bi ^[56,57] respectively have been observed in both cases however as additional peaks at around 388 and 689 eV are found only for $\text{P}@\text{Bi}_2\text{Se}_3$. The pair of peaks ascribed to Bi 4f and Se 3P at a binding energy of ~160 eV overlap each nevertheless the intensity of peak corresponding to Bi 4f transition is much higher than that of Se 3P.^[54–56] To throw more light on the structural exploration of the sample high-resolution spectrum pertaining the key elements have been deconvoluted and examined. As shown in Figure 1(e), the Bi 4f transition exhibits two strong peaks at 157.8 and 163.2 eV that correspond to the binding energies of Bi 4f_{7/2} and Bi 4f_{5/2} and in Figure 1(f), Se 3d_{5/2} and Se 3d_{3/2} transitions are ascribed to the peaks located at 54.2 and 57.6 eV respectively^[55] however there is a satellite peak observed at 56.2 eV assigned to SeO_x due to surface oxidation upon exposure to atmosphere, a common phenomenon found in metal chalcogenides including Bi_2Se_3 .^[58]

As it is evident from the deconvoluted high-resolution spectrum of Bi (P@Bi₂Se₃) Figure 1(g), there are two additional exceptional humps observed at 159.6 and 164.9 eV besides the signature peaks pertaining to Bi 4f_{7/2} (157.4 eV) and Bi 4f_{5/2} (162.8 eV). These extra peaks in P@Bi₂Se₃ at 159.6 and 164.9 eV designate Se 3p_{3/2} and Se 3p_{1/2} transitions respectively.^[57] Conversely the high-resolution of selenium in P@Bi₂Se₃ (Figure 1h) exhibits a unified peak instead of a doublet observed in the case of Bi₂Se₃. The 3d_{5/2} and 3d_{3/2} transitions of selenium positioned at 54.2 and 57.6 eV respectively in the case of Bi₂Se₃ have undergone a negative shift (3d_{5/2}-53.7 eV and 3d_{3/2}-55.5 eV). On the contrary the shoulder peak corresponding to SeO_x found in pristine Bi₂Se₃ disappeared after phosphorization, as the heat supplied would have caused the exit of excess unreacted selenium. The incorporation of P into the layers of Bi₂Se₃ is confirmed from the 2p_{3/2} and 2p_{1/2} transitions at the

binding energies of 134.2 and 136.5 eV respectively which match well with the literature (Figure 1i).^[59] A separate high-resolution scan of oxygen was carried out to understand the extent of surface oxidation in the prepared sample. As depicted in Figure S2(a) the peak at 529.3 eV can be associated with the binding energy of the O 3d_{3/2} transition. In the case of the P@Bi₂Se₃ sample, intercalation of phosphorous has played an interventional role by bringing in notable changes. Oxygen absorption from in atmosphere is detected in P@Bi₂Se₃ too as a peak noticed at 532.4 eV can be indexed to O 3d_{3/2} transition as shown in Figure S2(b). The results inferred from the XPS spectrum correlate well with the XRD analysis confirming the formation of Bi₂Se₃ and P@Bi₂Se₃.

Figure 2 represents the scanning electron (SEM) micrographs of as synthesized 3D bulk Bi₂Se₃ and P@Bi₂Se₃. Figure 2(a, a-i, a-ii) exhibits the SEM images of Bi₂Se₃ in different

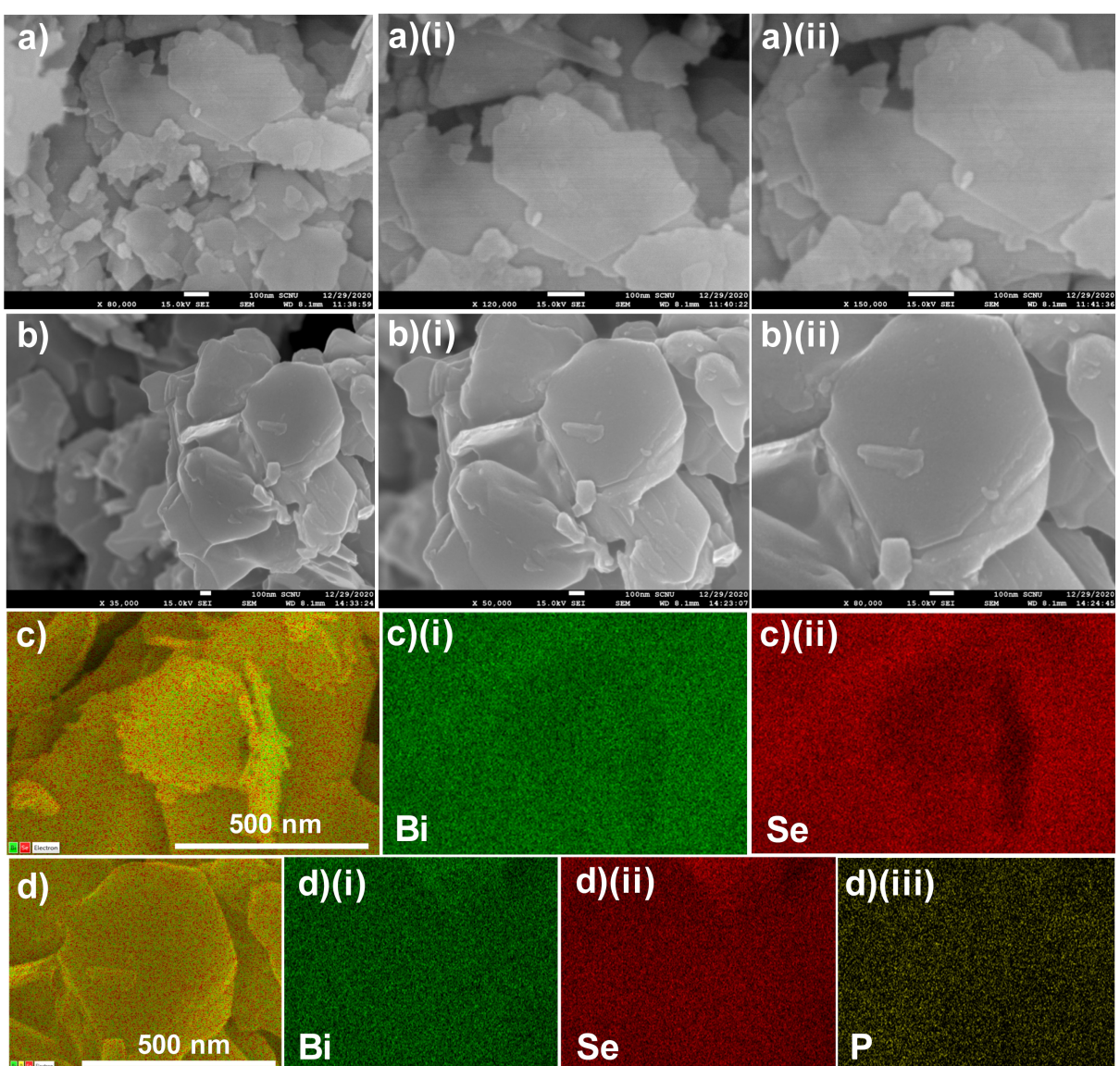


Figure 2. a, a-i and a-ii) The FE-SEM images at different magnification of Bi₂Se₃, b, b-i and b-ii) The FE-SEM images at different magnification of P@Bi₂Se₃, c, c-i, c-ii) FE-SEM EDX elemental mapping images of Bi₂Se₃ and d, d-(i-iii)) FE-SEM EDX elemental mapping images of P@Bi₂Se₃.

magnifications shows layered nature of the as synthesized 3D bulk Bi_2Se_3 and these platelets like layers that are stacked along the c -axis resembling sedimentary rock like morphology. In the quintuple layer comprising of five atoms the coupling within covalent bonding holds the individual layers together. The anisotropic structure and the coordinating solvent used dictate the growth mechanism to form layered structure. The seed crystal formed initially^[60] prefer to grow along the top-bottom planes rather than along c -axis since growth on the low-index planes can reduce the surface energy.^[61] Therefore, 2D Bi_2Se_3 sheets are formed and stacked together rather than 3D architecture. The advantage with our work is obtaining large and thin sheets of Bi_2Se_3 by simple hydrothermal method using water as solvent without using any additional stabilizing/capping agent except HMT. The formation of Bi_2Se_3 starts with covalent bond formation between Bi–Bi and Bi–Se which serve as the building blocks to form the individual layer by making an extended network. The formation of covalent bond between the adjacent layers is absent since the orbital of valence electrons lie inside the layer and hence the growth with anisotropic crystal formation takes place in top-bottom. Such layers grown during the reaction, get stacked vertically along c -axis and held together by van der Waals forces. HMT does its dual role as a reducing agent and stabilizing agent to occupy the van der Waals voids and facilitate the growth of along top-down direction and not along c -axis promoting preferential growth of 2D layers. The intercalation of P carried out at 350°C not only incorporated P but also caused annealing effect to $\text{P@Bi}_2\text{Se}_3$ as it is evident from the increase in peak intensities in the XRD. The effect of annealing along with phosphorization can be seen from the SEM images shown in Figure 2(b, b-i, b-ii) with different magnifications. The surface morphology of the individual Bi_2Se_3 layers remained intact without undergoing significant transformation even after intercalating of P at elevated temperature. Moreover, the stacked architecture also is retained however some level of fusing has occurred due to heating at 350°C leaving behind improved crystallinity as observed in XRD (Figure 1a, b). The surface morphology of Bi_2Se_3 -A, with better crystalline nature than $\text{P@Bi}_2\text{Se}_3$, closely resembles that of $\text{P@Bi}_2\text{Se}_3$ (Figure S3a, a-i, a-ii), revealing retention of layered structure with heat induced fused surface morphology. When compared to Bi_2Se_3 , Bi_2Se_3 -A and $\text{P@Bi}_2\text{Se}_3$ samples exhibit the effect of heat in terms of fused structure. The elemental mapping recorded for Bi_2Se_3 (Figure 2c, c-i, c-ii), Bi_2Se_3 -A (Figure S3b, b-i, b-ii) and $\text{P@Bi}_2\text{Se}_3$ [Figure 2d, d(i–iii)] support for the claims from XRD and XPS analysis for the formation of Bi_2Se_3 and $\text{P@Bi}_2\text{Se}_3$. In all the three cases (Bi_2Se_3 , Bi_2Se_3 -A and $\text{P@Bi}_2\text{Se}_3$) the uniform distribution of compositional elements all over the sample is confirmed. From EDS, the La peaks pertaining to Bi, Se and O indicate that the compound formed is Bi_2Se_3 (Bi_2Se_3 and Bi_2Se_3 -A) composed of Bi and Se with certain amount of atmospheric oxidation (Figure S4a and b). Similarly, for $\text{P@Bi}_2\text{Se}_3$ sample incorporation of P is confirmed along with Bi, Se and O (Figure S4c). The detected O atoms will be found mainly on the surface of the layers since the composition of the bulk samples show close stoichiometry of Bi_2Se_3 Bi_2Se_3 -A and $\text{P@Bi}_2\text{Se}_3$ in the bulk and no other peaks

indicative of oxide compounds are observed in XRD as well. Further investigation on the structural morphology using TEM add additional evidence for the layered structure of Bi_2Se_3 comprising of stacked 2D individual layers (Figure 3a). The high-resolution TEM (HR-TEM) image (Figure 3a-i) and the selected area electron diffraction (SAED) pattern (inset of Figure 3a-i) clearly indicate the 2D layered structure with high crystallinity of Bi_2Se_3 . As depicted in Figure 3(a-ii) and inset, the detailed analysis lattice fringes with d -spacing ≈ 0.264 nm (Average for 10 fringes as shown Figure 3a-iii) corresponding (015) plane of hexagonal Bi_2Se_3 and fast Fourier transform (FFT) vouch for the crystalline nature of the material. The images of $\text{P@Bi}_2\text{Se}_3$ show the retention of layered structure (Figure 3b) even after phosphorization and the improved crystallinity due to heat applied during phosphorization can be observed from the SAED pattern (Figure 3b-i and inset). Interestingly the lattice fringes of $\text{P@Bi}_2\text{Se}_3$ pertaining to (015) plane (Figure 3b-ii and inset) have expanded up to ≈ 0.370 nm from 0.264 nm (Average for 10 fringes as shown in Figure 3b-iii). The increase in d spacing of (015) plane can be ascribed to the intercalation of P matching well with the peak shift observed in XRD pattern. Figure 3[c, c(i–iii), d, d(i–iv)] represents the elemental mapping and the EDX spectrum Bi_2Se_3 and $\text{P@Bi}_2\text{Se}_3$ respectively. The elemental mapping reveals homogenous distribution of constituent elements for both Bi_2Se_3 (Bi and Se) and $\text{P@Bi}_2\text{Se}_3$ (Bi, Se and P), supporting the observation made in FE-SEM EDX analysis.

Based on the above results on the structural and morphological properties the electrocatalytic profile of Bi_2Se_3 and $\text{P@Bi}_2\text{Se}_3$ through electrochemical measurements were carried out for understanding and evaluating their intrinsic electrocatalytic capability to explore the possibility of employing them as electrodes in supercapacitor. The electrodes for the electrochemical studies were prepared as described earlier and coated on nickel foam (NF) and hence the electrodes will be denoted as $\text{Bi}_2\text{Se}_3/\text{NF}$, $\text{P@Bi}_2\text{Se}_3/\text{NF}$ and the electrochemical measurements were performed using a three-electrode cell configuration in alkaline electrolyte (6 M KOH). Cyclic voltammetry (CV) scans were carried out in the potential range from 0.0 to 0.55 V at a scan rate of 10 mV s⁻¹ for the $\text{Bi}_2\text{Se}_3/\text{NF}$ and $\text{P@Bi}_2\text{Se}_3/\text{NF}$ electrodes along with NF for comparison. The CVs recorded shown in Figure 4(a) for both $\text{Bi}_2\text{Se}_3/\text{NF}$ and $\text{P@Bi}_2\text{Se}_3/\text{NF}$ reveal notable redox peaks however the former exhibited a pair of redox peaks pertaining to battery like Faradaic behavior^[14,62] and the latter possessed much larger enclosed area of CV and highest peak current intensity registering its superior capacitive nature. The total charge (C) is the product of current (A) and time (s) and therefore increase in scan rate results in reduced time leading to increase in the current. So, the enclosed area of the CV swells with increased scan rate. To complement the claim for the better electrochemical profile of $\text{P@Bi}_2\text{Se}_3/\text{NF}$ from P intercalation, CV was carried out under identical conditions for Bi_2Se_3 -A/NF compared with the counter parts (Figure S5a). Bi_2Se_3 -A/NF demonstrated similar CV profile with meager increase in the current density and a slight shift in the redox peaks but possessed low catalytic behavior when compared to $\text{P@Bi}_2\text{Se}_3$. Therefore, the notable capacitance revealed by

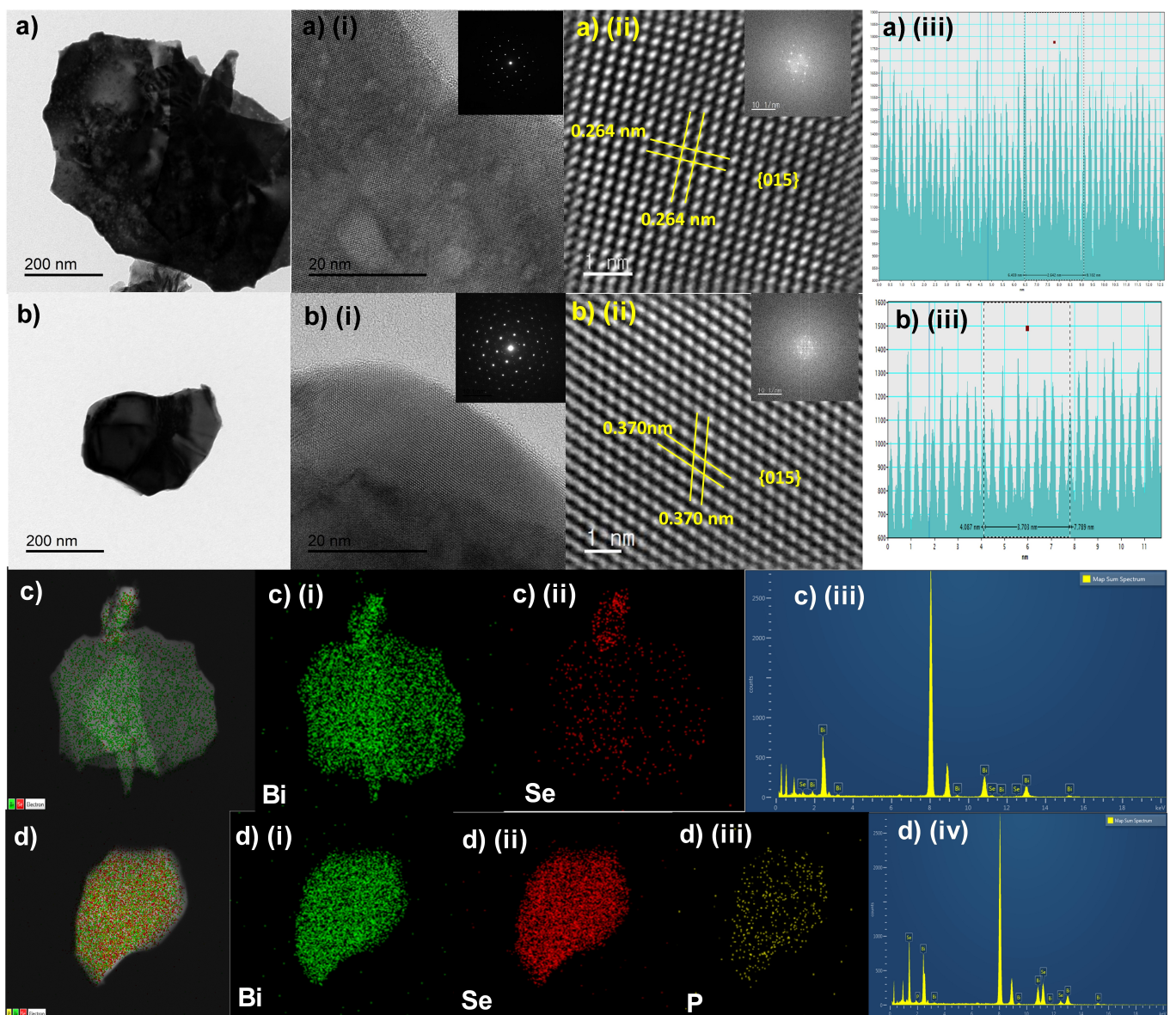
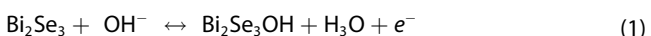


Figure 3. a) Typical TEM, a-i) HR-TEM (inset: SAED pattern), a-ii) High resolution images (inset: FFT pattern), a-iii) lattice fringes measurement of Bi_2Se_3 . b) TEM, b-i) HR-TEM (inset: SAED pattern), b-ii) high resolution images (inset: FFT pattern), b-iii) Lattice fringes measurement of $\text{P}@\text{Bi}_2\text{Se}_3$. c, c-i and c-ii) EDX elemental mapping images, c-iii) EDX spectrum of Bi_2Se_3 , d, d-(i-iii)) EDX elemental mapping images, d-(iv)) EDX spectrum of $\text{P}@\text{Bi}_2\text{Se}_3$.

$\text{P}@\text{Bi}_2\text{Se}_3/\text{NF}$ is not just due to heat assisted crystallinity but also due to combined effect from localized surface plasmon resonance induced by P and increased charge carrier concentration, intercalated P enacting as catalytic centers and easy passage via wide interlayer spacing with P intercalation. The ample active sites available on the surface of the Bi_2Se_3 layers contribute to the increase in capacitance by faradaic reactions in KOH as presented in Equation (1).



The reaction type and its kinetics governing the overall redox reaction of the electrocatalyst can be analyzed using the power-law by determining the value of b using Equations (2) and (3).^[63]

$$i = av^b \quad (2)$$

$$\log i = \log a + b \log v \quad (3)$$

where i and v represent current (A) and scan rate (V s^{-1}), respectively, a is a variable and b is the slope of the fitted line obtained for $\text{P}@\text{Bi}_2\text{Se}_2$ from the plot of $\log v$ vs. $\log i$ at a fixed potential (V) as depicted in Figure S5(b). The value of b is calculated from the fitted linear plot and the value of b normally lies between 0.5 to close to 1. As shown in Figure S5(c) the value of b obtained for $\text{P}@\text{Bi}_2\text{Se}_2$ lies at 0.87 for a potential of 0.25 V and upon increase in the voltage b value oscillates and therefore predicting the exact behavior of the electrode material remains ambiguous. Therefore, in order to draw a clear insight on the reaction kinetics the correlation

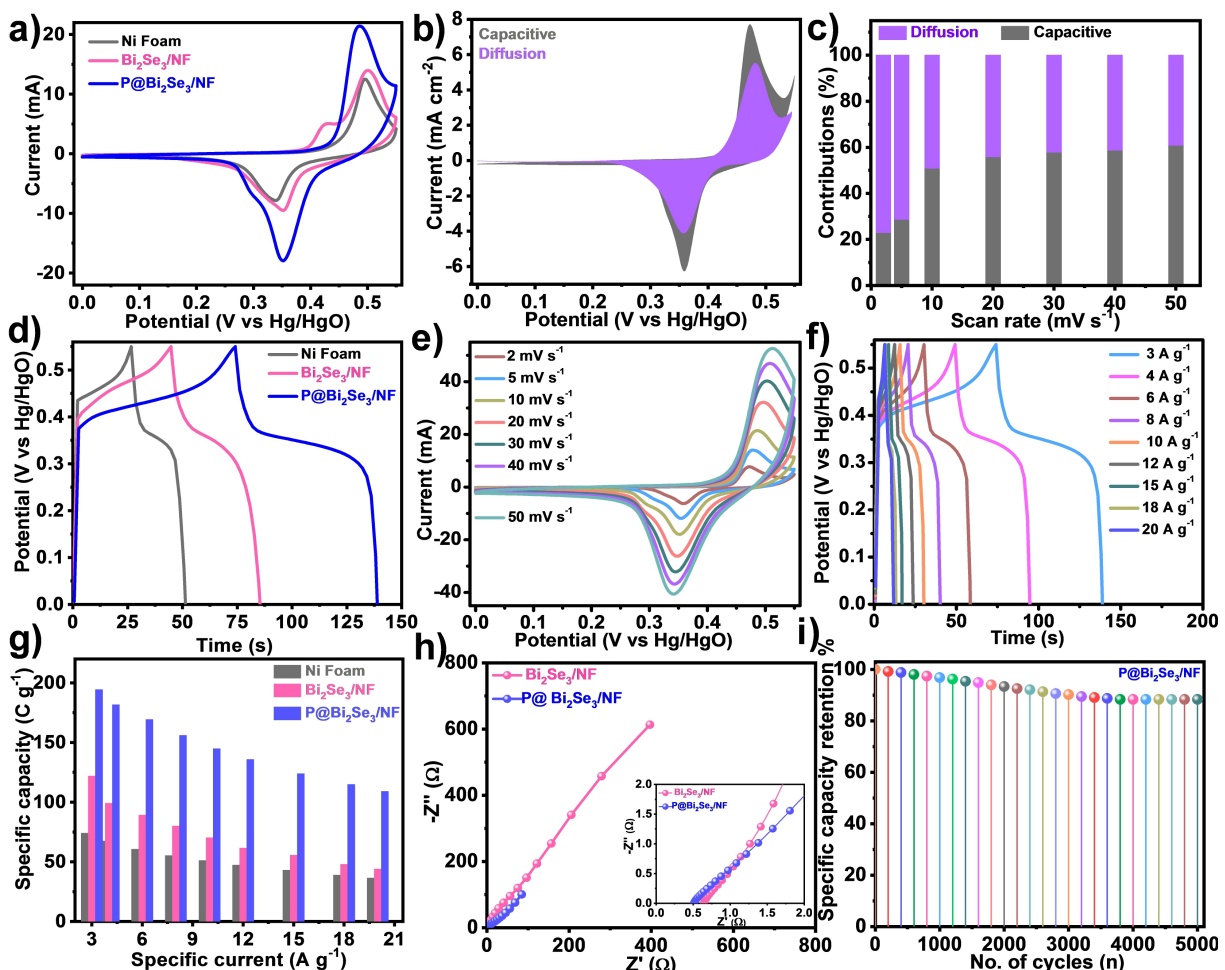


Figure 4. a) CV curves of NF, $\text{Bi}_2\text{Se}_3/\text{NF}$ and $\text{P}@\text{Bi}_2\text{Se}_3/\text{NF}$ electrodes at a scan rate of 10 mV s^{-1} , b) intercalation and capacitive charge contributions of $\text{P}@\text{Bi}_2\text{Se}_3/\text{NF}$ electrode at a scan rate of 2 mV s^{-1} , c) percentage contributions of intercalation and capacitive charge storage for $\text{P}@\text{Bi}_2\text{Se}_3/\text{NF}$ at different scan rates of $2, 5, 10, 20, 30, 40$ and 50 mV s^{-1} , d) comparative GCD profiles of NF, $\text{Bi}_2\text{Se}_3/\text{NF}$ and $\text{P}@\text{Bi}_2\text{Se}_3/\text{NF}$ electrodes at different specific current of 3 A g^{-1} , e) CVs of $\text{P}@\text{Bi}_2\text{Se}_3/\text{NF}$ electrode measured at different scan rates of $2, 5, 10, 20, 30, 40$ and 50 mV s^{-1} , f) GCD curves of $\text{P}@\text{Bi}_2\text{Se}_3/\text{NF}$ electrode measured at different specific currents of $3, 4, 6, 8, 10, 12, 15, 18$ and 20 A g^{-1} , g) The variation of specific capacity (C_s) values of the NF, $\text{Bi}_2\text{Se}_3/\text{NF}$, and $\text{P}@\text{Bi}_2\text{Se}_3/\text{NF}$ electrodes at different currents of $3, 4, 6, 8, 10, 12, 15, 18$ and 20 A g^{-1} , h) Nyquist plots of $\text{Bi}_2\text{Se}_3/\text{NF}$ and $\text{P}@\text{Bi}_2\text{Se}_3/\text{NF}$ electrodes (inset shows the magnified view at high-frequency region) and i) cyclic stability of the $\text{P}@\text{Bi}_2\text{Se}_3/\text{NF}$ electrode over 5000 cycles at 5 A g^{-1} .

between capacitive and diffusion-controlled contribution to the total capacity was determined using Equations (4) and (5):^[64–66]

$$i(V) = K_1 v + K_2 v^{1/2} \quad (4)$$

where $i(V)$ represents the potential dependent current, $K_1 v$ is the surface capacitive contribution and $K_2 v^{1/2}$ is the diffusion-controlled contribution. In order to find out the values of K_1 and K_2 , the above Equation (4) is modified as Equation (5).

$$\frac{i(V)}{v^{1/2}} = K_1 v^{1/2} + K_2 \quad (5)$$

As represented in Figure S5(d) the slope and intercept form the linear fit from plot $v^{1/2}$ vs. $i(V)/v^{1/2}$ correspond to K_1 and K_2 respectively. Applying the calculated values of K_1 and K_2 in Equation (3) the percentage of charge storage contribution in terms of capacitive and intercalation mechanism is obtained.

Figure 4(b) displays the capacitive and diffusion-controlled contribution to the capacitance by $\text{P}@\text{Bi}_2\text{Se}_3/\text{NF}$ electrode. Figure 4(c) exhibits the plot between capacitance vs. scan rate, and it can be noted that at the scan rate of 2 mV s^{-1} , 23% of the capacitive controlled contribution and 77% diffusion-controlled contribution is observed. When increasing the scan rate the capacitive controlled contribution increased to 60% at the scan rate of 50 mV s^{-1} which indicates that the electrochemical reaction dictated by diffusion at low scan rates and even at high scan rates nearly 40% of diffusion is retained. It implies that the wide interlayer spacing between the adjacent Bi_2Se_3 layers due to intercalation of P permit easy diffusion of electrolytes contributing significantly to the overall capacitance. The GCD behavior of NF, $\text{Bi}_2\text{Se}_3/\text{NF}$ and $\text{P}@\text{Bi}_2\text{Se}_3/\text{NF}$ electrodes at 3 A g^{-1} in the voltage window of 0 – 0.55 V is shown in Figure 4(d) and the nonlinear shape of the $\text{Bi}_2\text{Se}_3/\text{NF}$ and $\text{P}@\text{Bi}_2\text{Se}_3/\text{NF}$ electrodes inform their faradaic current profile^[67] and $\text{P}@\text{Bi}_2\text{Se}_3/\text{NF}$ exhibits highest discharge time. Hence the

GCD behavior of P@Bi₂Se₃/NF electrode confirms its high capacitance output which correlates with its CV profile. On the contrary the GCD performance of Bi₂Se₃-A/NF is far behind both Bi₂Se₃/NF and P@Bi₂Se₃/NF (Figure S5e) indicating that the fused structure by simple annealing without P intercalation, hampers the electrocatalytic behavior. Figure 4(e) depicts the CV of P@Bi₂Se₃/NF electrode for different scan rates from 2–50 mV s⁻¹ and it can be seen from it the progressive increase in its current with increase in the scan rates. Furthermore, the shape of the curve and the signature redox peaks have been preserved throughout the different scan rates which indicates the stable and consistent performance of the electrode. The CVs recorded for P@Bi₂Se₃/NF electrode at different scan rates from 2 to 50 mV s⁻¹ display the retention of signature redox peaks with intactness of shape and battery like behavior even at higher scan rate.^[68] The GCD behavior of P@Bi₂Se₃ recorded at various current densities (3, 4, 6, 8, 10, 12, 15, 18 and 20 A g⁻¹) are shown in Figure 4(f) and it is observed that all the GCD curves are symmetric in nature and nonlinear while, upon increasing the current densities, the discharge times decreases. At high current densities the charge/discharge process occurs much faster than at low current densities. Therefore, during fast charge/discharge the electrolyte ions do not have sufficient time to cover the catalyst surface yielding nonlinear GCD curves upon increasing the current density. The specific capacity calculated from GCD curves at 3 A g⁻¹ from the graph (Figure 4g) are 74, 121 and 194 C g⁻¹ for NF and P@Bi₂Se₃/NF, respectively, where P@Bi₂Se₃ seemed to exhibit highest specific capacity suggesting the contribution from P intercalation and the eventual inducement in surface plasmon resonance, high carrier concentration and expansion in interlayer spacing. High carrier concentration aids to boost catalytic activity, conductivity and increased interlayer spacing provides enhanced transport. The capacity of Bi₂Se₃-A/NF, calculated from the GCD curves obtained at 3 A g⁻¹ is only 106 C g⁻¹ (Figure S5f), lying far behind pristine Bi₂Se₃. So, the P intercalation has a significant role in escalating the electrocatalytic profile of the Bi₂Se₃. Similar CV and GCD studies conducted for NF and Bi₂Se₃/NF and Bi₂Se₃-A/NF for comparison have been shown in Figure S6(a-f). To support the said claims on the aforementioned electrocatalytic activity and to infer further insight EIS analysis was carried out in 6 M KOH aqueous solution to evaluate their resistance behavior and capacitive behavior and the corresponding Nyquist plots for Bi₂Se₃ and P@Bi₂Se₃ fitted using Z View software are shown in Figure 4(h) and that of bare Ni foam and Bi₂Se₃-A/NF electrodes are shown in Figure S7(a and b) respectively and the insets show the equivalent circuit used to fit. The impedance curves were fitted with an equivalent circuit and the fitted parameters are presented in Table 1. The equivalent circuit used for fitting consists of internal or solution resistance (R_s) which is the intersection of real axis at high-frequency region, charge-transfer resistance (R_{ct}), double layer capacitance (C_{dl}), pseudocapacitance (C_p), and Warburg resistance (W_R) of the redox electrolyte. The solution resistance (R_s), charge-transfer resistance (R_{ct}) calculated for P@Bi₂Se₃/NF electrode (0.4644 and 0.644 Ω cm²) is much lower than that of Bi₂Se₃/NF (0.5122 and 0.685 Ω cm²), Bi₂Se₃-A/NF

Table 1. EIS fitted parameters of NF, Bi₂Se₃ and P@Bi₂Se₃ electrodes, and P@Bi₂Se₃//O, N, S@AC HSC before and after cyclic stability.

Parameters	R_s [Ω cm ²]	R_{ct} [Ω cm ²]	C_{dl} [F cm ⁻²]	C_p [F cm ⁻²]	W_R [Ω cm ²]
NF	0.588	1.496	0.006	0.0076	0.42752
Bi ₂ Se ₃ /NF	0.5122	0.685	0.01	0.015	0.2571
Bi ₂ Se ₃ -A/NF	0.8154	0.749	0.045	0.02	0.371
P@Bi ₂ Se ₃ /NF	0.4644	0.644	0.025	0.033	0.070
O, N, S @AC/NF	0.2702	0.273	0.822	0.223	0.484
P@Bi ₂ Se ₃ /NF // O,N,S@AC/NF (Before 10,000 cycles)	6.3	0.1848	0.8723	5.406	0.3782
P@Bi ₂ Se ₃ /NF // O,N,S@AC/NF (After 10,000 cycles)	6.53	0.280	0.9358	9.99	0.4242

(0.8154 and 0.749 Ω cm²) and NF (0.588 and 1.496 Ω cm²), respectively, suggesting superior electrochemical behavior with enhanced electronic and ionic conductivity and charge transfer process by P@Bi₂Se₃/NF owing to the architecture. In traditional layered architectures the interlayer spacing usually offers good electron pathway channels however such a phenomenon is boosted upon expanding the inter layer spacing by some means of altering. As compared to NF and Bi₂Se₃/NF, because of epitaxial engineered surface of P@Bi₂Se₃/NF electrode with P atoms intercalation it acquires abundance of active sites both on the surface of the layers and in the interlayer spacing as well. Besides that, the minute increase in the interlayer spacing associated with the insertion of P atoms and promotion of charge carriers with surface plasmon resonance enhancement cater-effective redox performance at the electrode/electrolyte interfaces, rapid ion diffusion and piling of electrolytic ions on electrode surface.^[69,70] The Warburg resistance (W_R) observed in the mid-frequency region with a spike angle of 45° is associated with ion diffusion process^[71] and appreciable transport and diffusion of ions in the case of P@Bi₂Se₃/NF electrode is related to negligible values of W_R . Moreover, the cyclic stability was carried out for the best performing P@Bi₂Se₃/NF electrode exhibits retention of nearly 88% of initial specific capacity over 5000 charge/discharge cycles (Figure 4i). With the proven cyclic stability and excellent reversibility of the champion P@Bi₂Se₃/NF electrode, it is further analyzed for device performance by assembling a hybrid supercapacitor (HSC). The electrochemical profile of O, N, S@AC/NF electrode was studied in order to examine its suitability as a negative electrode before employing it for assembling HSC. A set of experiments were performed such as CVs, GCD, and impedance for O, N, S@AC/NF electrode in 6 M KOH aqueous electrolyte. The CVs conducted at different scan rates in the voltage window of 0.0–1.0 V presented in Figure S8(a) possess rectangular shape and reveal its electric double-layer capacitance (EDLC). Besides that, the enrichment of O, N and S in the active carbon is exhibited in the form of meager amount to pseudocapacitance. The GCD curves carried out at different current densities (1–15 A g⁻¹) as shown in Figure S8(b) provide additional confirmation for the EDLC with triangle shaped curve however pseudocapacitance caused certain amount of deformation in shape. The C_s values for the said electrode

calculated from GCD using Equation (7) for O, N, S@AC/NF electrode are 328, 267, 240, 227, 218, 212, 206 and 198 F g^{-1} , at 1, 2, 4, 6, 8, 10, 12, and 15 A g^{-1} , respectively (Figure S8c and d). The impedance measurement conducted, and the parameters obtained from corresponding fitted Nyquist plot ($R_s = 0.2707 \Omega \text{ cm}^2$ and $R_{ct} = 0.273 \Omega \text{ cm}^2$) additionally support for the capacitive profile of O, N, S@AC/NF.^[72] Therefore HSC was fabricated using P@Bi₂Se₃/NF and O, N, S @AC/NF^[35] as positive and negative electrodes, respectively. The electrochemical profile of the HSC was tested by performing CV, GCD and EIS and the obtained results are presented in Figure 5. The CVs recorded in the potential window of 0 to 0.55 V for P@Bi₂Se₃/NF and 0 to -1 V for O, N, S @AC/NF electrodes (Figure 5a) at the scan rate of 10 mVs⁻¹. To fabricate the efficient HSC the mass balance equation was used for regulating the mass of electrodes using Equation (6):^[73]

$$\frac{m_+}{m_-} = \frac{C_- \times \Delta V_-}{C_+} \quad (6)$$

where ' m_+ ' and ' m_- ', ' C_- ' and ' C_+ ', and ' ΔV_- ' are the active electrode mass, specific capacity and specific capacitance of the positive and negative electrodes capacitance and specific capacity of negative and positive electrodes and voltage window of negative electrode, respectively. The mass ratio between P@Bi₂Se₃/NF (1.560 mg) and O, N, S @AC/NF (1.162 mg) was optimized to 1:1.34 so that the total mass of the active material loaded on both electrodes was adjusted to 2.77 2.722 mg for the complete HSC. The CV profile of O, N, S@AC/NF electrode shows that it possesses rectangular shape corresponding to pseudocapacitance while the characteristics of P@Bi₂Se₃/NF portray battery like behavior and each of them display a stable capacitance profile in their respective potential window. Figure 5(b and c) depicts the comparative CVs of P@Bi₂Se₃/NF//O, N, S @AC/NF at a scan rate of 25 mVs⁻¹

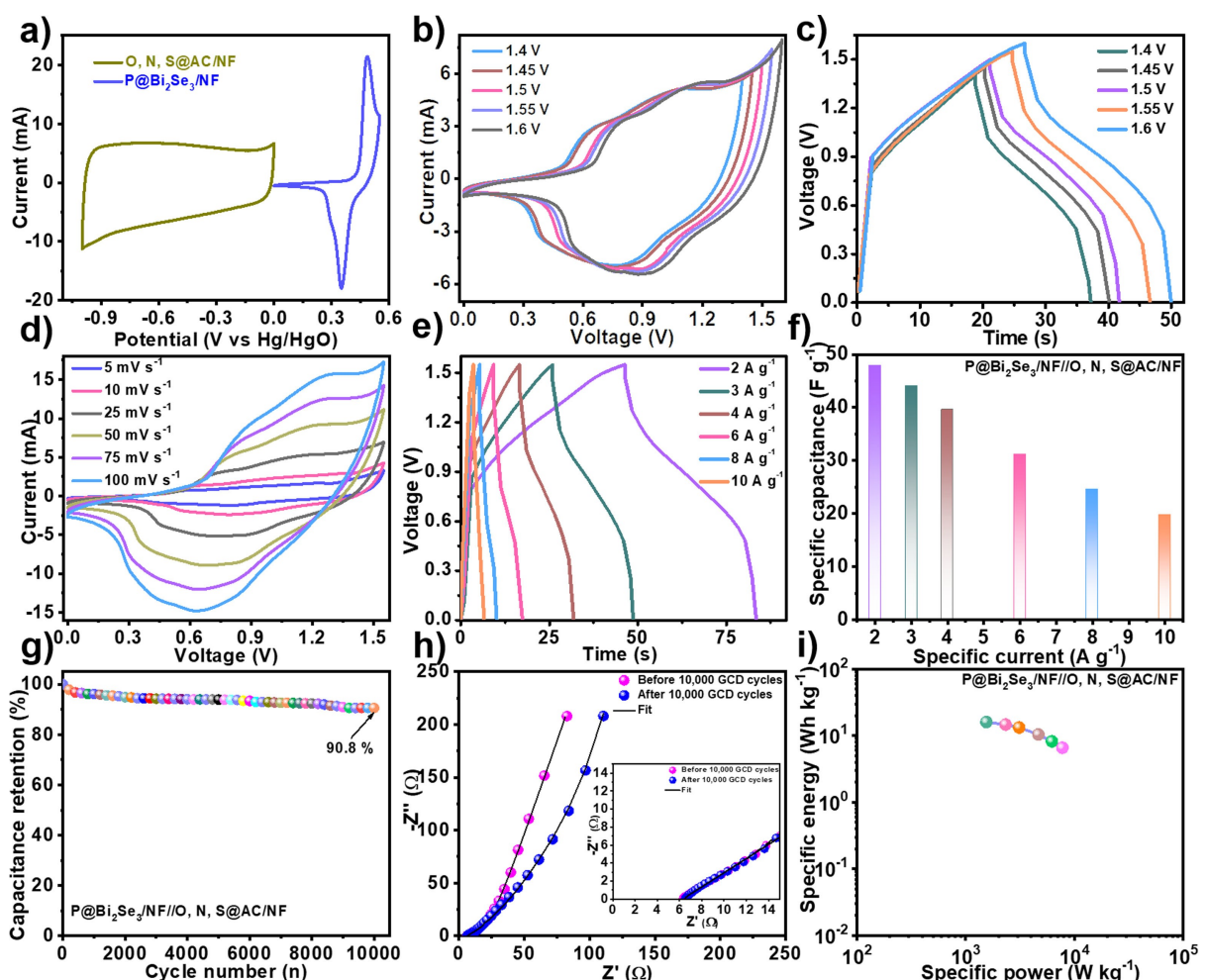


Figure 5. a) CVs of positive electrode (P@Bi₂Se₃/NF) and negative electrode (O, N, S@AC/NF) half-cell at a scan rate of 10 mVs⁻¹, b) CVs of HSC device made of P@Bi₂Se₃//O, N, S@AC electrodes for different potential windows (1.4–1.6 V) at a scan rate of 25 mVs⁻¹, c) GCD curves of HSC device under different potential windows (1.4–1.6 V) at a specific current of 3 Ag⁻¹, d) CVs of HSC measured at different scan rates of 5, 10, 25, 50, 75 and 100 mVs⁻¹, e) GCD curves of HSC measured at different specific currents of 2, 3, 4, 6, 8, and 10 Ag⁻¹, f) variation of device specific capacitance with current densities of 2, 3, 4, 6, 8, and 10 Ag⁻¹, g) cycling stability of HSC for 10,000 cycles at a current density of 5 Ag⁻¹, h) Nyquist plots of HSC investigated before and after 10,000 charge/discharge cycles and the inset shows magnified view and i) Ragone plot for HSC device.

and GCD at a current density of 3 A g^{-1} respectively at a different voltage range of 1.4–1.6 V. The CV plots for different voltages for the HSC configuration exhibits high peak current along with large enclosed area and upon increasing the voltage the shape of the CV and GCD curves have been well maintained proving the stability of the electrodes throughout the voltage increment at an optimal voltage of 1.55 V the HSC shows almost symmetric curve with excellent capacitance delivery. The CVs of HSC measured at different scan rates from 5–100 mVs⁻¹ shown in Figure 5(d) exhibits a quasi-rectangular shape arising from the combined contribution from pseudocapacitance from O, N, S @AC/NF and battery-type capacitance from P@Bi₂Se₃/NF electrodes respectively. The reversibility and intactness of CVs have been preserved upon increasing the scan rates from 5–100 mVs⁻¹ however the enclosed area increased with increase in scan rate. Further supervision on the GCD characteristics of the HSC carried out for different current densities of 2, 3, 4, 6, 8, and 10 A g⁻¹ in the voltage window of 0 to 1.55 V in 6 M KOH solution is presented in Figure 5(e). The GCD curves of the HSC exhibited outstanding electrochemical reversibility and possessed quasi symmetrical shape at the specific current density of 2 A g^{-1} . The specific capacitance (C_s) of the HSC has been calculated using Equation (7) and the respective bar diagram is shown in Figure 4(f).

$$C_s (\text{F g}^{-1}) = \frac{I \times \Delta t}{m \times \Delta V} \quad (7)$$

where I represents discharge current (A), Δt denotes the discharge time expresses in seconds (s) and m is the mass of the active material constituting the electrode (g).

The specific capacitance (C_s) of HSC is 47, 44, 39, 31, 24 and 19 F g⁻¹ for the specific current densities of 2, 3, 4, 6, 8 and 10 A g⁻¹ respectively. The consistent performance of the HSC was evaluated by examining its long-time cyclic stability at a constant specific current of 5 A g^{-1} for 10000 continuous GCD cycles and the result shown in Figure 5(g) reveals that the device retained about 90.8% of the original specific capacitance at 10000th cycle evidencing its excellent reversibility and withstanding capacity. The EIS measurement for the HSC device before and after cyclic stability test adds further support to the outstanding reversible behavior of the device. Figure 5(h) shows the fitted data of Nyquist plots corresponding to the EIS measurements and the inset shows EIS spectra at high magnification at small values of (0–15 Ω). The EIS parameters obtained from the fit data given in Table 1 shows negligible increase in R_s (6.3–6.53 Ω cm²) after cyclic test. Similarly, the insignificant changes in R_{ct} and W_R values vouch for the stable behavior of the fabricated device with only 10.05% drop in the original capacitance. The specific and power density of the HSC can be calculated using Equations (8) and (9):

$$E_s = \frac{I \times \int \Delta V(t) \times dt}{m \times 3.6} \quad (8)$$

$$P_s = \frac{E_s \times 3600}{dt} \quad (9)$$

where E_s represents specific energy (Wh kg⁻¹), P_s denotes the specific power (W kg⁻¹), and $\int V(t)dt$ is the integral of GCD discharge curve area. The Ragone plot of the device plotted between E_s vs. P_s shown in Figure 5(i) evidences for the performance of HSC showcases that an excellent E_s of 15.9 Wh kg⁻¹ corresponding to the P_s value of 1550 W kg⁻¹ at the current density of 2 A g^{-1} and reveals maximum P_s of 7750 W kg⁻¹ for the E_s reading of 6.5 Wh kg⁻¹ at a high specific current of 10 A g^{-1} once again validating the superior electrochemical performance of HSC comprised of P@Bi₂Se₃//O, N, S@AC. When compared to the recently published research works^[74–76] on similar materials the capacitive behavior exhibited by P@Bi₂Se₃//O, N, S@AC is better or comparable suggesting the suitability of P@Bi₂Se₃ for energy storage application.

To demonstrate the feasibility for real-time applications coin cell assembly using HSC composition was fabricated as shown in Figure 6(a), and two such cells were connected serially (Figure 6b and c). The commercial 15 light-emitting diodes (LEDs) of green (~2 V) and red (~1.6 V) colors were connected parallelly to display "Bi" pattern (Figure 6c) was arranged to manifest device ability light up the LED pattern. The serially connected coin cell when connected to the set up LED pattern, the discharge voltage illuminated it with high specific power and specific energy, illustrating the capability of the P@Bi₂Se₃//O, N, S@AC electrodes to be employed for energy storage utilization (Figure 6d-i, d-ii, e-i, e-ii). The outstanding electrocatalytic profile of P@Bi₂Se₃ can be attributed to i) epitaxial engineering strategy to introduce P in between the Bi₂Se₃ layers and on their surface and the eventual escalation of localized surface plasmon resonance resulting increase in charge carrier concentration ii) the P atoms introduced acting as catalytic centers and iii) the increase in interlayer space facilitating easy accessibility and quick exodus of the electrolytic ions.

Conclusion

In summary, 2D stacked Bi₂Se₃ with graphene like architecture was synthesized by one step hydrothermal method and its surface was epitaxial engineering by introduce P atoms by CVD. The incorporation of P atoms boosted the existing LSPR properties further that reflected in the electrochemical behavior. Benefiting from epitaxial engineering via P intercalation and LSPR, P@Bi₂Se₃/NF delivered a specific capacity (C_s) of 194 C g^{-1} at 3 A g^{-1} current density against 121 C g^{-1} by Bi₂Se₃/NF and 106 C g^{-1} by Bi₂Se₃-A/NF under the same condition and P@Bi₂Se₃/NF retained 88% of its initial specific capacity beyond 5000 charge/discharge cycles. The HSC fabricated using P@Bi₂Se₃//O, N, S@AC delivered a maximum C_s of 47 F g^{-1} at a current density of 2 A g^{-1} with 90.8% of capacitance retention over 10000 continuous GCD cycles, demonstrating the effect of

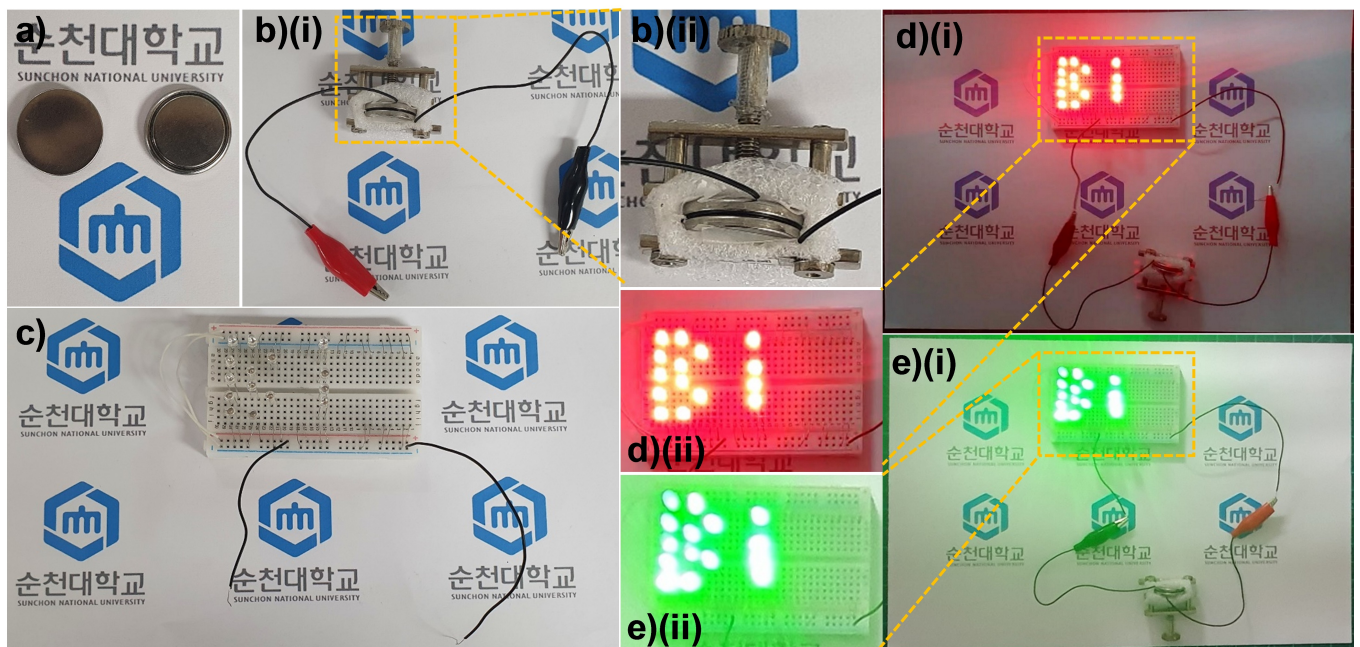


Figure 6. Photographic images of a) HSC fabricated with P@Bi₂Se₃/NF and O, N, S@AC/NF electrodes using coil cell assembly b-i) serially connected HSC coin cells and b-ii) its magnification, c) B1 LEDs pattern, the serially connected HSC lighting d-i) 15 red color LEDs and e-i) 15 green color LEDs (B1 pattern) after charging and d-ii and e-ii) their respective magnifications.

P intercalation. In addition, the device fabricated showed high E_s of 15.9 Wh kg⁻¹ and P_s of 7750 W kg⁻¹ at a current density of 2 and 10 A g⁻¹ respectively. The outstanding electrochemical performance of P@Bi₂Se₃ is because of the availability of high ion-accessible surface area. Besides the large surface area of the layered Bi₂Se₃, the escalation in the electrocatalytic profile of P@Bi₂Se₃ is ascribed to i) the amplification of localized surface plasmon resonance and increased charge carrier concentration with the intercalation of P, ii) surface-phosphorization translated catalytic centers and iii) expansion of interlayer space offering rapid transport of electrolyte ions. We believe that this electrocatalyst developed with non-precious materials can be a suitable cost-effective alternative. This work further paves a way for the choice of P@Bi₂Se₃ as an ideal alternative candidate towards energy storage devices. We envisage this epitaxial engineering strategy by incorporating guest atoms in layered materials can be extended for many other potential applications beyond energy storage.

Experimental Section

Reagents

Bismuth nitrate pentahydrate [Bi(NO₃)₃·5H₂O], carbon black and polyvinylidene fluoride (PVDF) were purchased from Alfa Aesar, Germany, Hexamethylenetetramine (C₆H₁₂N₄) (HMT), selenium powder (100 mesh, ≥99.5% trace metals basis), sodium hypophosphite monohydrate (NaPO₂H₂.H₂O), potassium hydroxide (KOH), and N-methyl-2-pyrrolidone (NMP) were obtained from Sigma-Aldrich. All the chemicals were used of analytical grade without further purification.

Synthesis of layered Bi₂Se₃ structures

Initially, ~46 mM of Bi(NO₃)₃·5H₂O was dissolved in 40 mL of deionized (DI) water under constant stirring for 20 min. Then ~80 mM of HMT was also added to the above solution and stirred continuously to achieve uniform solution. To this solution, 0.465 g of selenium powder was added and stirred to obtain homogenous depression and the resulting solution was transferred to 50 mL Teflon liner and placed in the stainless-steel autoclave. The hydrothermal set up was kept in a hot air oven and subjected to heat treatment at 180 °C for 24 h. The Bi₂Se₃ obtained in the form of black precipitate was washed several times in DI water and centrifuged to reach a neutral pH (=7) and finally washed with ethanol. The resulting Bi₂Se₃ precipitate was dried in vacuum oven at 60 °C for 12 h and used for further phosphorization process. The obtained sample is labelled Bi₂Se₃ and used for further modification and experiments.

Surface phosphorization of Bi₂Se₃

Surface phosphorization of Bi₂Se₃ was carried out in a tubular furnace (SH Scientific) under inert atmosphere (Argon). About 0.5 g of the as prepared Bi₂Se₃ and 1 g of NaPO₂H₂.H₂O was loaded in two different silica boats separately which were kept 5 cm apart from each other. Phosphorization was achieved by supplying a heat at 350 °C for 1.5 h with a heating rate of 5 °C min⁻¹ under Ar atmosphere and cooled to room temperature (RT) at the rate of 1 °C min⁻¹. In order to elucidate the effect of phosphorization on the electrocatalytic behavior and make a comparison, another 0.5 g of Bi₂Se₃ was subjected to annealing at identical condition (at 350 °C for 1.5 h under Ar atmosphere) without NaPO₂H₂.H₂O. The P intercalated sample and the annealed samples are labelled as P@Bi₂Se₃ and Bi₂Se₃-A respectively.

Fabrications of supercapacitor electrodes and hybrid supercapacitor (HSC)

The Ni foams ($1 \times 2.5 \text{ cm}^2$) was pretreated with 10% of HCl solution for a period of 15 min and washed with DI water, ethanol, acetone, and isopropanol under sonication and dried overnight at 60°C in a vacuum oven. The slurry for electrode was prepared by grinding 75% of the catalyst (Bi_2Se_3 or $\text{Bi}_2\text{Se}_3\text{-A}$ or $\text{P@Bi}_2\text{Se}_3$ or AC), 25% carbon black and 5% of polyvinylidene fluoride (PVDF) in a mortar with NMP as solvent. The prepared slurry was coated on the pretreated Ni foam within $1 \times 1 \text{ cm}^2$ and allowed to dry overnight at 60°C in a vacuum oven. For the fabrication of HSC positive and negative electrodes were prepared by coating $\text{P@Bi}_2\text{Se}_3$ and O, N, S@AC^[35] (prepared as per our earlier report) respectively on Ni foam substrate. The positive and negative electrodes were sandwiched by placing them vis-a-vis keeping a cellulose filter paper (Whatman filter paper 42) soaked in 6 M KOH in between them to serve as separator. Stainless-steel split test cell (EQ-STC) procured from MTI Korea Ltd. was used to assemble the HSC by incorporating $\text{P@Bi}_2\text{Se}_3$ and AC coated Ni foam substrate as positive and negative electrodes, respectively.

Structural characterization

The crystallinity and structural profiles of the synthesized materials (Bi_2Se_3 , $\text{Bi}_2\text{Se}_3\text{-A}$ and $\text{P@Bi}_2\text{Se}_3$) have been analyzed using by X-ray diffraction (XRD, D/max-2400, Rigaku, Ultima IV) with Cu K_α source operated at 30 mA and 40 kV with the 2θ values in the range of 10° – 90° . Optical properties were analyzed using a Jasco V-570, UV-vis-NIR spectrophotometer in the range of 200–1200 nm using absorbance mode. Versa probe II spectrometer was used to carryout X-ray photoelectron spectroscopy (XPS) measurement using Al K_α radiation. The morphology and the elemental pattern of Bi_2Se_3 , $\text{Bi}_2\text{Se}_3\text{-A}$ and $\text{P@Bi}_2\text{Se}_3$ have been captured using Hitachi-S4800 model field-emission scanning electron microscopy (FE-SEM) operated at an accelerating voltage of 3 kV. The detailed morphological analysis and elemental mapping of Bi_2Se_3 and $\text{P@Bi}_2\text{Se}_3$ were characterized using high-resolution transmission electron microscope (HR-TEM) JEOL model JEM-2100F (Japan).

Electrochemical measurements

The electrochemical studies for the electrocatalysts prepared were conducted using VSP Biopotentiostat/galvanostat (BioLogic) electrochemical workstation (France) at RT ($\sim 25^\circ\text{C}$). The electrochemical performances of the synthesized electrodes (three electrode cell) and hybrid supercapacitor were tested using cyclic voltammetry (CV) for different scan rates galvanostatic charge-discharge tests (GCD) for different specific current densities and electrochemical impedance spectroscopy (EIS) for the frequency range of 10 mHz–100 kHz under 0 V bias voltage with a sinus amplitude of 10 mV were performed using 6 M KOH aqueous electrolyte. Three-electrode system consist of the $\text{Bi}_2\text{Se}_3/\text{NF}$, $\text{Bi}_2\text{Se}_3\text{-A}/\text{NF}$ and $\text{P@Bi}_2\text{Se}_3/\text{NF}$ samples coated on Ni foam served as working electrode while platinum (Pt) coiled wire and Hg/HgO have been used as counter and reference electrodes at RT in 6 M KOH aqueous electrolyte.

Credit authorship contribution statement

Antony Samy Dennyson Savariraj: Conceptualization, Designing the manuscript, Writing-original draft – review & editing . Ramu Manikandan: Supporting experiments, designing rough structure, Writing – review & editing. C. Justin Raj: Supporting experiments, Writing – review & editing. Rajavel Velayutham: Supporting experi-

ments, designing rough structure, Validation, Visualization, Writing – review & editing. R.V.Mangalaraja: Designing rough structure, Validation, Writing – review & editing. Jinsoo Park: Supporting experiments, Validation, Writing – review & editing. Won-Je Cho: Project administration, Supervision, Validation, Visualization, Writing – review & editing. Byung Chul Kim: Project administration, Supervision, Validation, Visualization, Writing – review & editing.

Declaration of competing interest

The authors declare that they have no known competing financial interests or personal relationships that could have appeared to influence the work reported in this research article.

Acknowledgements

This research was supported by Basic Science Research Program through the National Research Foundation of Korea (NRF) funded by the Ministry of Education (NRF-2014R1A6A1030419) and by the National Research Foundation of Korea (NRF) Grant funded by the Korean government (MSIT) (No. 2020112382).

Conflict of Interest

The authors declare no conflict of interest.

Keywords: bismuth selenide · chemical vapor deposition · epitaxial engineering · hybrid supercapacitor · localized surface plasmon resonance

- [1] M. Naguib, V. N. Mochalin, M. W. Barsoum, Y. Gogotsi, *Adv. Mater.* **2014**, *26*, 992–1005.
- [2] A. K. Geim, K. S. Novoselov, *Nat. Mater.* **2007**, *6*, 183–191.
- [3] T. Xiong, M. Zhu, Y. Zhang, W. S. V. Lee, Z. G. Yu, J. Xue, *Batteries & Supercaps* **2020**, *3*, 519–526.
- [4] X. Wang, K. Du, Y. Y. Fredrik Liu, P. Hu, J. Zhang, Q. Zhang, M. H. S. Owen, X. Lu, C. K. Gan, P. Sengupta, C. Kloc, Q. Xiong, *2D Mater.* **2016**, *3*, 031009.
- [5] K. Du, X. Wang, Y. Liu, P. Hu, M. I. Utama, C. K. Gan, Q. Xiong, C. Kloc, *ACS Nano* **2016**, *10*, 1738–1743.
- [6] J. Liu, X. Li, D. Wang, W. Lau, P. Peng, L. Liu, *J. Chem. Phys.* **2014**, *140*, 054707.
- [7] X. Zhang, X. Zhao, D. Wu, Y. Jing, Z. Zhou, *Adv. Sci.* **2016**, *3*, 1600062.
- [8] C. Kuo, M. Neumann, K. Balamurugan, H. J. Park, S. Kang, H. W. Shiu, J. H. Kang, B. H. Hong, M. Han, T. W. Noh, J. Park, *Sci. Rep.* **2016**, *6*, 20904.
- [9] X. Li, X. Wu, J. Yang, *J. Am. Chem. Soc.* **2014**, *136*, 11065–11069.
- [10] X. Wang, M. Pi, D. Zhang, H. Li, J. Feng, S. Chen, J. Li, *ACS Appl. Mater. Interfaces* **2019**, *11*, 14059–14065.
- [11] M. Pumera, A. H. Loo, *TrAC Trends Anal. Chem.* **2014**, *61*, 49–53.
- [12] K. Alitabar, A. M. Zardkhoshouei, S. S. Hosseiny Davarani, *Batteries & Supercaps* **2020**, *3*, 1311–1320.
- [13] R. Gusmão, Z. Sofer, D. Sedmidubský, Š Huber, M. Pumera, *ACS Catal.* **2017**, *7*, 8159–8170; Huber, M. Pumera, *ACS Catal.* **2017**, *7*, 8159–8170.
- [14] Z. Chen, Y. Yang, Z. Ma, T. Zhu, L. Liu, J. Zheng, X. Gong, *Adv. Funct. Mater.* **2019**, *29*, 1904182.
- [15] V. Amendola, *Phys. Chem. Chem. Phys.* **2016**, *18*, 2230–2241.
- [16] A. D. Savariraj, K. K. Viswanathan, K. Prabakar, *ACS Appl. Mater. Interfaces* **2014**, *6*, 19702–19709.
- [17] A. D. Savariraj, H. Kim, K. K. Viswanathan, M. Vijaykumar, K. Prabakar, *RSC Adv.* **2016**, *6*, 19034–19040.

- [18] A. D. Savariraj, V. Vinoth, R. V. Mangalaraja, T. Arun, D. Contreras, A. Akbari-Fakhrabadi, H. Valdés, F. Banat, *J. Electroanal. Chem.* **2020**, *856*, 113629.
- [19] X. Liu, C. Lee, W. Law, D. Zhu, M. Liu, M. Jeon, J. Kim, P. N. Prasad, C. Kim, M. T. Swihart, *Nano Lett.* **2013**, *13*, 4333–4339.
- [20] M. J. Manos, N. Ding, M. G. Kanatzidis, *Proc. Natl. Acad. Sci. USA* **2008**, *105*, 3696.
- [21] M. Manos, M. Kanatzidis, *Chem. Eur. J.* **2009**, *15*, 4779–4784.
- [22] R. Singh, P. Kumari, M. Kumar, T. Ichikawa, *A. Molecules Jain.* **2020**, *25*, 3733.
- [23] Y. Zhang, K. He, C. Chang, C. Song, L. Wang, X. Chen, J. Jia, Z. Fang, X. Dai, W. Shan, S. Shen, Q. Niu, X. Qi, S. Zhang, X. Ma, Q. Xue, *Nat. Phys.* **2010**, *6*, 584–588.
- [24] B. Pejova, I. Grozdanov, A. Tanuševski, *Mater. Chem. Phys.* **2004**, *83*, 245–249.
- [25] J. Guozhi, W. Peng, Z. Yanbang, C. Kai, *Sci. Rep.* **2016**, *6*, 25884.
- [26] P. Flouda, X. Feng, J. G. Boyd, E. L. Thomas, D. C. Lagoudas, J. L. Lutkenhaus, *Batteries & Supercaps* **2019**, *2*, 464–472.
- [27] L. M. Abrantes, J. P. Correia, *Surf. Coat. Technol.* **1998**, *107*, 142–148.
- [28] E. J. Popczun, J. R. McKone, C. G. Read, A. J. Biacchi, A. M. Wiltrot, N. S. Lewis, R. E. Schaak, *J. Am. Chem. Soc.* **2013**, *135*, 9267–9270.
- [29] D. Mukherjee, M. A. P. S. Sampath, *ACS Appl. Energ. Mater.* **2018**, *1*, 220–231.
- [30] B. Zhou, Y. Zhao, L. Pu, J. Zhu, *Mater. Chem. Phys.* **2006**, *96*, 192–196.
- [31] Z. Ding, S. K. Bux, D. J. King, F. L. Chang, T. Chen, S. Huang, R. B. Kaner, *J. Mater. Chem.* **2009**, *19*, 2588–2892.
- [32] J. Bludská, I. Jakubec, S. Karamazov, J. Horák, C. Uher, *J. Solid State Chem.* **2010**, *183*, 2813–2817.
- [33] H. Yoo, K. Heo, M. H. Ansari, S. Cho, *Nanomaterials* **2021**, *11*.
- [34] Y. Li, C. Xu, P. Hu, L. Zhen, *ACS Nano* **2013**, *7*, 7795–7804.
- [35] R. Manikandan, C. J. Raj, S. E. Moulton, T. S. Todorov, K. H. Yu, B. C. Kim, *Chem. Eur. J.* **2021**, *27*, 669–682.
- [36] L. Sun, Z. Lin, J. Peng, J. Weng, Y. Huang, Z. Luo, *Sci. Rep.* **2014**, *4*, 4794.
- [37] K. Paraskevopoulos, E. Hatzikraniotis, K. Chrisafis, M. Zamani, J. Stoemenos, N. A. Economou, K. Alexiadis, M. Balkanski, *Mater. Sci. Eng. B* **1988**, *1*, 147–154.
- [38] K. Mazumder, A. Sharma, Y. Kumar, P. M. Shirage, *Phys. Chem. Chem. Phys.* **2018**, *20*, 28257–28266.
- [39] S. Yang, P. Zhang, A. S. Nia, X. Feng, *Adv. Mater.* **2020**, *32*, 1907857.
- [40] C. Lei, Q. Zheng, F. Cheng, Y. Hou, B. Yang, Z. Li, Z. Wen, L. Lei, G. Chai, X. Feng, *Adv. Funct. Mater.* **2020**, *30*, 2003000.
- [41] I. Jeon, B. Yoon, M. He, T. M. Swager, *Adv. Mater.* **2018**, *30*, 1704538.
- [42] S. Yang, M. R. Lohe, K. Müllen, X. Feng, *Adv. Mater.* **2016**, *28*, 6213–6221.
- [43] K. Parvez, Z. Wu, R. Li, X. Liu, R. Graf, X. Feng, K. Müllen, *J. Am. Chem. Soc.* **2014**, *136*, 6083–6091.
- [44] Y. Min, G. D. Moon, B. S. Kim, B. Lim, J. Kim, C. Y. Kang, U. Jeong, *J. Am. Chem. Soc.* **2012**, *134*, 2872–2875.
- [45] A. Ambrosi, Z. Sofer, J. Luxa, M. Pumera, *ACS Nano* **2016**, *10*, 11442–11448.
- [46] J. Zhou, Q. Lin, H. Li, X. Cheng, *Mater. Chem. Phys.* **2013**, *141*, 401–405.
- [47] C. Lu, X. Li, Q. Wu, J. Li, L. Wen, Y. Dai, B. Huang, B. Li, Z. Lou, *ACS Nano* **2021**, *15*, 3529–3539.
- [48] J. M. Luther, P. K. Jain, T. Ewers, A. P. Alivisatos, *Nat. Mater.* **2011**, *10*, 361–366.
- [49] S. Ghosh, M. Saha, S. K. De, *Nanoscale* **2014**, *6*, 7039–7051.
- [50] X. Yang, X. Wang, Z. Zhang, *J. Cryst. Growth* **2005**, *276*, 566–570.
- [51] P. H. Le, K. H. Wu, C. W. Luo, J. Leu, *Thin Solid Films* **2013**, *534*, 659–665.
- [52] J. Fu, S. Song, X. Zhang, F. Cao, L. Zhou, X. Li, H. Zhang, *CrystEngComm* **2012**, *14*, 2159–2165.
- [53] M. DC, J. Chen, T. Peterson, P. Sahu, B. Ma, N. Mousavi, R. Harjani, J. Wang, *Nano Lett.* **2019**, *19*, 4836–4844.
- [54] Z. Sun, S. Liufu, L. Chen, *Dalton Trans.* **2010**, *39*, 10883–10887.
- [55] V. B. Nascimento, V. E. de Carvalho, R. Paniago, E. A. Soares, L. O. Ladeira, H. D. Pfannes, *J. Electron Spectrosc. Relat. Phenom.* **1999**, *104*, 99–107.
- [56] H. Xu, G. Chen, R. Jin, D. Chen, J. Pei, Y. Wang, *CrystEngComm* **2013**, *15*, 5626–5632.
- [57] X. Wang, C. M. Smyth, A. Khosravi, C. R. Cormier, J. R. Shallenberger, R. Addou, R. M. Wallace, *Surf. Sci. Spectra* **2019**, *26*, 024014.
- [58] D. Kong, J. J. Cha, K. Lai, H. Peng, J. G. Analytis, S. Meister, Y. Chen, H. Zhang, I. R. Fisher, Z. Shen, Y. Cui, *ACS Nano* **2011**, *5*, 4698–4703.
- [59] Z. Wang, D. Kong, M. Wang, G. Wang, N. Li, D. Li, *RSC Adv.* **2019**, *9*, 12990–12997.
- [60] J. A. Hollingsworth, D. M. Poojary, A. Clearfield, W. E. Buhro, *J. Am. Chem. Soc.* **2000**, *122*, 3562–3563.
- [61] W. Lu, Y. Ding, Y. Chen, Z. L. Wang, J. Fang, *J. Am. Chem. Soc.* **2005**, *127*, 10112–10116.
- [62] G. Ma, F. Hua, K. Sun, E. Fenga, H. Peng, Z. Zhang, Z. Lei, *R. Soc. Open Sci.* **2018**, *5*, 171186.
- [63] P. Sivakumar, P. Nakhanivej, C. J. Raj, H. S. Park, *Int. J. Energy Res.* **2021**, *45*, 10832–10842.
- [64] M. Z. Iqbal, S. S. Haider, S. Siddique, M. R. A. Karim, S. Zakar, M. Tayyab, M. M. Faisal, M. Sulman, A. Khan, M. Baghayeri, M. A. Kamran, T. Alherbi, M. J. Iqbal, T. Hussain, *J. Energy Storage* **2020**, *27*, 101056.
- [65] S. Xia, S. Yu, L. Yao, F. Li, X. Li, F. Cheng, X. Shen, C. Sun, H. Guo, J. Liu, *Electrochim. Acta* **2019**, *296*, 746–754.
- [66] T. Gong, X. Lou, E. Gao, B. Hu, *ACS Appl. Mater. Interfaces* **2017**, *9*, 21839–21847.
- [67] A. Meng, X. Yuan, T. Shen, Z. Li, Q. Jiang, H. Xue, Y. Lin, J. Zhao, *J. Mater. Chem. A* **2019**, *7*, 17613–17625.
- [68] Y. Gogotsi, R. M. Penner, *ACS Nano* **2018**, *12*, 2081–2083.
- [69] L. Sun, C. Tian, Y. Fu, Y. Yang, J. Yin, L. Wang, H. Fu, *Chem. Eur. J.* **2014**, *20*, 564–574.
- [70] R. Manikandan, C. J. Raj, G. Nagaraju, M. Pyo, B. C. Kim, *J. Mater. Chem. A* **2019**, *7*, 25467–25480.
- [71] R. Manikandan, C. J. Raj, K. H. Yu, B. C. Kim, *Appl. Surf. Sci.* **2019**, *497*, 143778.
- [72] C. J. Raj, M. Rajesh, R. Manikandan, K. H. Yu, J. R. Anusha, J. H. Ahn, D. Kim, S. Y. Park, B. C. Kim, *J. Power Sources* **2018**, *386*, 66–76.
- [73] S. Yang, C. Wu, J. Cai, Y. Zhu, H. Zhang, Y. Lu, K. Zhang, *J. Mater. Chem. A* **2017**, *5*, 16776–16785.
- [74] J. Li, Q. Wu, G. Zan, *Eur. J. Inorg. Chem.* **2015**, *2015*, 5751–5756.
- [75] H. Xu, X. Hu, H. Yang, Y. Sun, C. Hu, Y. Huang, *Adv. Energy Mater.* **2015**, *5*, 1401882.
- [76] S. X. Wang, C. C. Jin, W. J. Qian, *J. Alloys Compd.* **2014**, *615*, 12–17.

Manuscript received: October 21, 2021

Revised manuscript received: November 29, 2021

Accepted manuscript online: December 12, 2021

Version of record online: January 18, 2022